

## Article

# El Niño–Southern Oscillation-Independent Regulation of Western North Pacific Tropical Cyclone Genesis

Danlei Jian <sup>1,\*</sup>, Haikun Zhao <sup>1,\*</sup>, Min Liu <sup>1</sup> and Ronghe Wang <sup>2</sup>

<sup>1</sup> College of Atmospheric Sciences, Nanjing University of Information Science and Technology, Nanjing 210044, China; min.liu@nuist.edu.cn

<sup>2</sup> Delta Water Institute, Nanjing 211800, China; wang.ronghe@delta.org.cn

\* Correspondence: 20211201089@nuist.edu.cn (D.J.); haikunzhao@nuist.edu.cn (H.Z.)

**Abstract:** As the most significant interannual signal in the tropical Pacific, the influence of ENSO on the interannual variability in TC genesis location in the western North Pacific (WNP) has received much attention in previous studies. This paper mainly emphasizes the underlying SST factors independent of the ENSO signal and explores how they modulate interannual tropical cyclone genesis (TCG) latitude variability. Our study finds that the meridional sea temperature gradient (SSTG) between the Kuroshio Extension and the WNP still has a significant effect on the interannual variability in the TCG latitude after removing the effect of ENSO ( $r = 0.6$ ). The interannual forecasts of the TCG latitude were effectively improved from 0.67 to 0.81 when the ENSO-independent SSTG and ENSO were regressed together in a multi-linear regression. We then propose an ENSO-independent physical mechanism affecting the TCG latitude. The equatorward (poleward) SSTG excited the positive (negative) Pacific–Japan telecorrelation pattern over the WNP, forming Rossby wave trains and propagating northward. A significant cyclonic vortex (anticyclonic vortex) with strong convective development (suppression) developed near 20° N, leading more TCs to the northern (southern) part of the WNP. These findings provide a new perspective for the prediction of the interannual variability in the TCG latitude.

**Keywords:** ENSO; tropical cyclone genesis; western North Pacific



**Citation:** Jian, D.; Zhao, H.; Liu, M.; Wang, R. El Niño–Southern Oscillation-Independent Regulation of Western North Pacific Tropical Cyclone Genesis. *Atmosphere* **2024**, *15*, 537. <https://doi.org/10.3390/atmos15050537>

Academic Editors: Yilun Chen, Shumin Chen, Mingsen Zhou, Weibiao Li and Aoqi Zhang

Received: 21 March 2024

Revised: 23 April 2024

Accepted: 26 April 2024

Published: 28 April 2024



**Copyright:** © 2024 by the authors. Licensee MDPI, Basel, Switzerland. This article is an open access article distributed under the terms and conditions of the Creative Commons Attribution (CC BY) license (<https://creativecommons.org/licenses/by/4.0/>).

## 1. Introduction

Tropical cyclones (TCs) are one of the most destructive natural phenomena on Earth. Among all of the ocean basins, the western North Pacific (WNP) is the most active region of TC genesis, accounting for approximately one-third of the global TC frequency [1,2]. Frequent TC activities have caused a large number of casualties and property losses in the coastal areas of East Asia [3,4]. Therefore, the change in WNP TC activities has been the focus of many research concerns. However, previous studies have mainly focused on the forecasting of WNP TC frequency [5,6], track [7,8] and intensity [9,10], with less concern about the variation in the TC genesis location. Indeed, considerable challenges remain in the short-to-medium-term forecasting of TC genesis locations [11]; especially in the context of global warming, the uncertainty in the change in TC genesis location is significantly amplified [4,12,13]. Therefore, a deeper understanding of the variability in TC genesis locations may be helpful for improving seasonal forecasts of TCs.

Since the late 1990s, the global climate regime has shifted from a warm phase to a cold phase, the amplitude and volatility of ENSO have weakened, Center Pacific (CP)-type ENSO and La Niña events are occurring frequently [14], and WNP TC activity has changed significantly [3,15,16]. With the poleward shift of the TC lifetime maximum intensity (LMI) latitude and genesis latitude detected in recent decades of observations [17–20], the TC genesis (TCG) latitude change has gradually gained more attention. Several studies have attributed the interdecadal variation in the TCG latitude to the results of interdecadal phase

shifts [21,22], while others have attributed it to the effects of tropical expansion under global warming [23–25]. Despite the efforts of previous studies, the climatic drivers of the TCG latitude poleward shift are still controversial.

In comparison, there have been few studies on the interannual variability in the TCG latitude. As the most important interannual signal in the tropical Pacific, the influence of the El Niño–Southern Oscillation (ENSO) on TC activity has been confirmed in previous studies [26–29]. Different phases and intensities of ENSO, as well as the diversity of ENSO, can have remarkable impacts on the changes in TC activity [30–34]. Although ENSO has no effect on TCG frequency [3,29], it can significantly change the TCG location by influencing the Walker circulation and the Hadley circulation [27–29]. During the strong El Niño (La Niña) years, westerly anomalies under El Niño forcing strengthened the cyclonic vortex in the southeast quadrant ( $0^{\circ}$ – $17^{\circ}$  N,  $140^{\circ}$ – $180^{\circ}$  E) and guided more TCs to form in this area; conversely, under the influence of the East Asian Trough (EAT) and the upper-level convergence caused by the subtropical high pressure (SPH), the frequency of TCs formed in the northwest quadrant ( $17^{\circ}$ – $30^{\circ}$  N,  $120^{\circ}$ – $140^{\circ}$  E) was significantly reduced.

Apart from ENSO, the tropical Indian Ocean also has an important impact on interannual change in the western Pacific and East Asia [35–37]. The decaying El Niño can induce anomalous warming in the tropical Indian Ocean and stimulate a “Matsuno–Gill Pattern” response, which excites equatorial Rossby and equatorial Kelvin wave responses over the Indian and Pacific Oceans, respectively [38,39]. Subsequently, the eastward-transported equatorial Kelvin waves excite a Pacific–Japan (P–J) pattern over the northwestern Pacific Ocean [40,41], which could affect TC generation [42–44]. Zheng et al. (2016) [45] further emphasized the effect of SST anomalies in the North Indian Ocean on the north–south meridional dipole distribution of WNP TCs. However, these studies do not distinguish tropical Indian Ocean SST impacts from ENSO.

Although previous studies have confirmed that ENSO is the main predictive source for interannual forecasts of the TCG latitude [46,47], fewer studies have mentioned the contribution of other SST factors in the interannual TCG latitude variability. The existence of SST drivers independent of ENSO remains unclear. Therefore, this paper focuses on the influence of the ENSO-independent SST on the interannual TCG latitude and presents the corresponding physical mechanisms. The rest of this paper is organized as follows. The data and methodology used in the paper are described in Section 2. Section 3.1 describes the relationship between the ENSO-independent SST and the interannual variability in the TCG latitude. Section 3.2 explains how the ENSO-independent SST modulates the interannual variability in the TCG latitude. A summary and discussion are given in Section 4.

## 2. Materials and Methods

### 2.1. Materials

Observational TC data from 1979 to 2020 were obtained from the Joint Typhoon Warning Center (JTWC) best track dataset, which includes latitude, longitude, and maximum sustained wind speed at 6 h intervals [48]. We concentrated on TCs with maximum sustained winds of  $\geq 34$  knot ( $\sim 17$  m s $^{-1}$ ) (e.g., named storms), and the latitude at which the TC first reaches 34 knot is defined as the TCG latitude. Additionally, we focused on the TC peak season from July to October, when  $\sim 70\%$  of WNP named storms occur climatologically.

Monthly mean sea surface temperature (SST) data are obtained from the National Oceanic and Atmospheric Administration’s (NOAA) Extended Reconstructed SST version 5 (ERSST-V5) with a horizontal resolution of  $2^{\circ} \times 2^{\circ}$  [49]. Monthly mean atmospheric data are obtained from the National Centers for Environmental Prediction–Department of Energy Reanalysis 2 (NCEP–DOE Reanalysis 2) [50] with a horizontal resolution of  $2.5^{\circ} \times 2.5^{\circ}$  and 17 vertical pressure levels from 1000 to 10 hPa, including variables such as horizontal wind fields and relative humidity. Monthly mean Outgoing Longwave Radiation (OLR) data are obtained from the NOAA polar-orbiting satellite grid, with a horizontal resolution of  $2.5^{\circ} \times 2.5^{\circ}$ .

The Niño-3.4 index is calculated from the regional average of SST anomalies in the equatorial eastern Pacific Ocean from 5° S to 5° N and 170° to 120° W and is provided by the NOAA ([https://psl.noaa.gov/gcos\\_wgsp/Timeseries/Nino34/](https://psl.noaa.gov/gcos_wgsp/Timeseries/Nino34/), accessed on 12 May 2023).

## 2.2. Methods

### a. Definition of Pacific–Japan Index

The Pacific–Japan telecorrelation pattern is a pressure seesaw between the WNP and Japan, which has a significant impact on the summer climate change in East Asia [51,52]. In this paper, we use the Pacific–Japan (P–J) index defined by Wakabayashi and Kawamura (2004) [53] to discuss the relationship between the ENSO-independent SSTG and the P–J teleconnection pattern. The formula is as follows:

$$PJ \text{ index} = [Z_{850}(35^\circ\text{N}, 155^\circ\text{E}) - Z_{850}(22.5^\circ\text{N}, 125^\circ\text{E})]/2 \quad (1)$$

where  $Z_{850}$  represents the geopotential height anomalies at an 850 hPa level.

### b. Wave-activity flux

In this paper, we use the wave activity flux (WAF) equation defined by Takaya and Nakamura (2001) [54] to determine the origin and propagation of ENSO-independent SSTG-excited Rossby wave trains. The formula is as follows:

$$WAF = \frac{1}{2|\bar{U}|} \left[ \bar{u}(\psi_x'^2 - \psi' \psi_{xx}') + \bar{v}(\psi_x' \psi_y' - \psi' \psi_{xy}') \right] \quad (2)$$

where  $\psi$  represents the streamfunction and  $U = (u, v)$  represents the horizontal wind. The overbar and the prime represent the climatological mean and an anomaly, respectively.

### c. Dynamic TC genesis potential index

Previous studies have shown that the dynamic genesis potential index (DGPI) displays greater skill in characterizing both interannual and interdecadal TC changes in the WNP compared to the GPI proposed by Emanuel and Nolan (2004) [55–58]. Therefore, we follow the definition of the DGPI by Wang and Murakami (2020) [59] to diagnose WNP TC genesis. The formula is as follows:

$$DGPI = (2 + 0.1V_{shear})^{-1.7} \left( 5.5 - \frac{\partial u_{500}}{\partial y} 10^5 \right)^{2.3} (5 - 20\omega)^{3.3} \left( 5.5 + |10^5 \eta| \right)^{2.4} e^{-11.8} - 1 \quad (3)$$

where  $V_{shear}$  is the magnitude of 200–850 hPa wind shear;  $\frac{\partial u_{500}}{\partial y}$  is the meridional gradient of zonal wind at 500 hPa;  $\omega$  is the 500 hPa vertical pressure velocity; and  $\eta$  is the 850 hPa absolute vorticity. Prior studies have shown that the DGPI is a useful TC proxy, especially in a changing climate.

### d. Removing ENSO

Since we focus on SST influences independent of ENSO, linear regression is used to exclude the ENSO signal [60], which is calculated as follows:

$$Y = aX + R \quad (4)$$

where  $Y$  is the dependent variable with sample size  $n$ ,  $X$  is the independent variable with sample size  $n$  that needs to be filtered out of  $Y$ ,  $a$  is the linear regression coefficient, and  $R$  is the regression residual of the dependent variable  $Y$  after removing the signal  $X$ .

e. Extracting interannual signals

The interannual time series is calculated by subtracting the low-pass-filtered time series from the raw time series [61]. The formula is as follows:

$$X_{interannual} = X - X_{interdecadal} \quad (5)$$

where  $X$  is the raw series with sample size  $n$ ,  $X_{interannual}$  is the interannual time series of the variable  $X$ , and  $X_{interdecadal}$  is the time series after low-pass filtering on the raw series (i.e., the interdecadal time series). Here, we use a 9-point sliding average as a low-pass filter:

$$X_{interdecadalj} = \frac{1}{9} \sum_{i=1}^9 x_{i+j-1} \quad , \quad j = 1, 2, \dots, n - 9 + 1 \quad (6)$$

f. Significance test

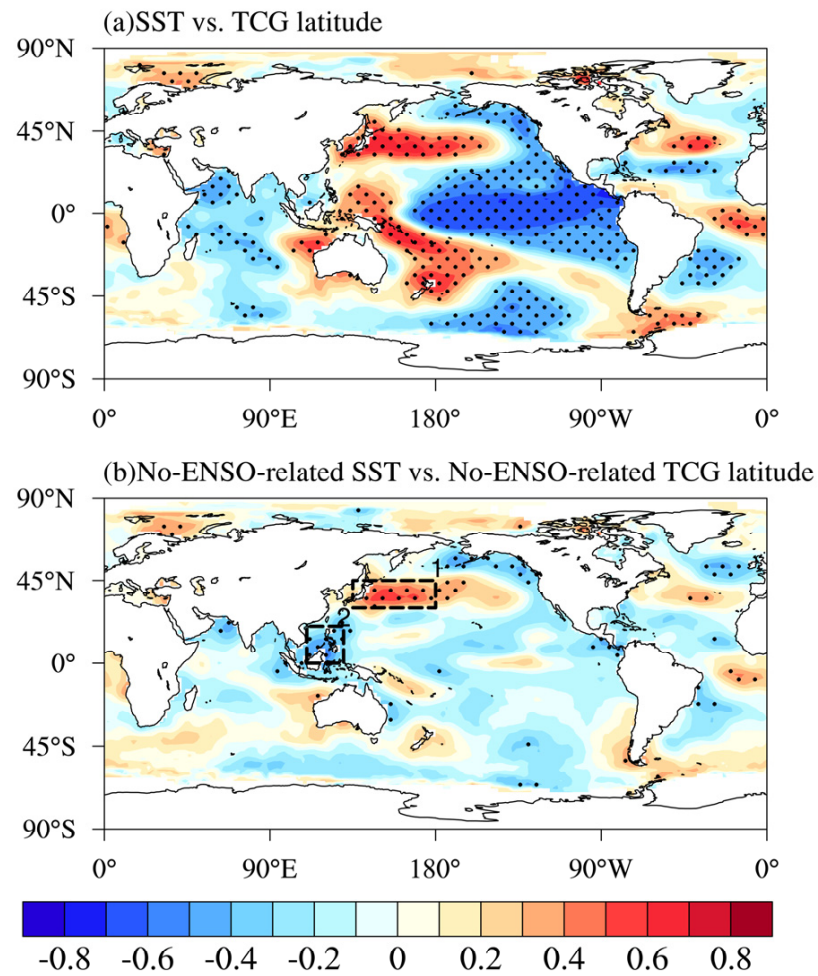
This paper uses the two-tailed Student's  $t$  test to check the significance of correlations and regression coefficients. Unless stated otherwise, only  $p$  values less than or equal to 0.05 are considered statistically significant.

### 3. Result and Discussion

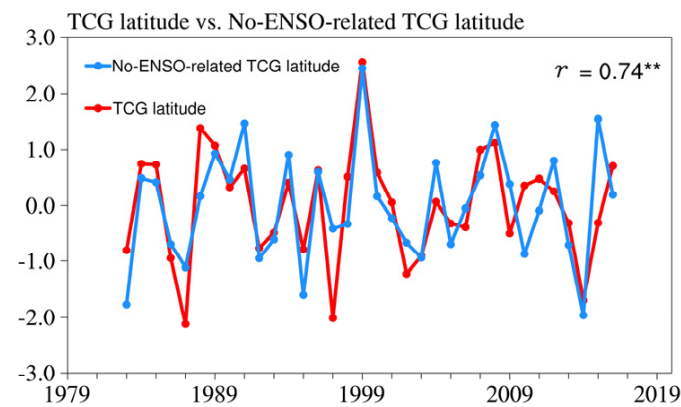
#### 3.1. Relationship between ENSO-Independent SST and Interannual Variability in TCG Latitude

Figure 1a shows the correlation between the global SST and the TCG latitude on interannual time scales from 1979 to 2020; the spatial correlation distribution in the Pacific displays an obvious La Niña-like pattern, which means that in El Niño years, the TCG latitude is southward, and in La Niña years, the TCG latitude is northward. Consistent with previous findings, this result emphasizes the primary contribution of ENSO to the interannual variation in the TCG latitude [27,28]. To examine the contribution of ENSO to the interannual TCG latitude, we removed the effect of ENSO from the TCG latitude and compared it to the time series of the TCG latitude without ENSO removal. From the results in Figure 2, we can easily find that the difference between the No-ENSO-related TCG latitude (blue line) and the TCG latitude (red line) is not significant, with a correlation coefficient of 0.74. Only a few years show a significant difference in the TCG latitude. That is, although ENSO contributes significantly to the interannual variability in the TCG latitude, there may be other SST factors affecting the interannual variability in the TCG latitude. This led us to focus not only on the effects of ENSO but also on other factors of SST variability in addition to ENSO.

In order to investigate the SST signal concealed by the strong ENSO, we next calculated the spatial correlation after removing the ENSO signal for both the TCG latitude and the SST. As shown in Figure 1b, after removing the impact of ENSO, a significant dipole correlation was detected between the Kuroshio Extension (KE) and the WNP, with a significant positive correlation in the KE region in contrast to a significant negative correlation south of 20° N in the WNP. In other words, under this meridional SST gradient of a warming north and cooling south, the mean TCG latitude is northward, whereas under the meridional SST gradient of a cooling north and warming north and south, the mean TCG latitude is southward. Previous studies have suggested that the effect of the WNP local SST on TC activity is mainly derived from remote forcing by ENSO and is insignificant after removing the effect of ENSO [27,62]. In contrast, here we emphasize the important effect of the WNP local SST on the TCG latitude variability. To quantify the effect of this dipole effect of the SST on the interannual TCG latitude variability, we calculated the regional mean SST for the KE (30°–45° N, 120°–180° E) and WNP (0°–20° N, 110°–130° E) and defined the KE regional mean SST minus the WNP regional mean SST after removing the ENSO signal as the ENSO-independent meridional SST gradient (SSTG).



**Figure 1.** (a) Spatial correlation between July and October mean TCG latitude and SST on the interannual time scale from 1979 to 2020. (b) As in (a), but the effects of ENSO on TCG latitude and SST are removed by linear regression. The black dots indicate significant correlations at the 95% confidence level. Black box 1 indicates the Kuroshio Extension region (30°–45° N, 120°–180° E), and black box 2 indicates the WNP region (0°–20° N, 110°–130° E).



**Figure 2.** Interannual standardized time series of July–October mean No-ENSO-related TCG latitude (blue line) and TCG latitude (red line) from 1979 to 2020. Two asterisks (\*\*) indicate that the correlation coefficients are significant at the 99% confidence level.

Subsequently, to validate the relationship between this new index and the TCG latitude, we calculated the correlation between the ENSO and ENSO-independent SSTGs and the TCG latitude (Figure 3). It can be seen that although ENSO still dominates the interannual

TCG latitude variability ( $r = -0.67$ ), the ENSO-independent SSTG shows a non-negligible contribution with a correlation coefficient of 0.6. This suggests that the index we define effectively reflects the effect of ENSO-independent SST variability on TCG latitude changes. Due to the close correlation between the ENSO-independent SSTG and the TCG latitude, we wondered if it could be used as a new forecasting factor to improve interannual forecasts of the TCG latitude. We performed multiple linear regressions of the TCG latitude using the ENSO-independent SSTG and ENSO to explore their contributions to the interannual variability in the TCG latitude. We first fitted the TCG latitude with ENSO and the ENSO-independent SSTG, respectively. As shown in Figure 4a,b, the correlation coefficients between the linear-fitted TCG latitude and the observations are 0.67 and 0.52 for the ENSO and ENSO-independent SSTGs, which explain 44.9% and 27% of the interannual variation in the TCG latitude, respectively. In addition, when the ENSO and ENSO-independent SSTGs were regressed together as independent predictors in a multiple linear regression (Figure 4c), the correlation coefficient of the linearly fitted TCG latitude with observations increased to 0.81, increasing the explained variance by 20.7% and collectively explaining 65.6% of the interannual variation in the TCG latitude. That is, the ENSO-independent SSTG as a new predictor significantly improves the interannual forecast of the TCG latitude. These results emphasize the important role of the ENSO-independent SSTG in regulating the interannual variability in the TCG latitude.

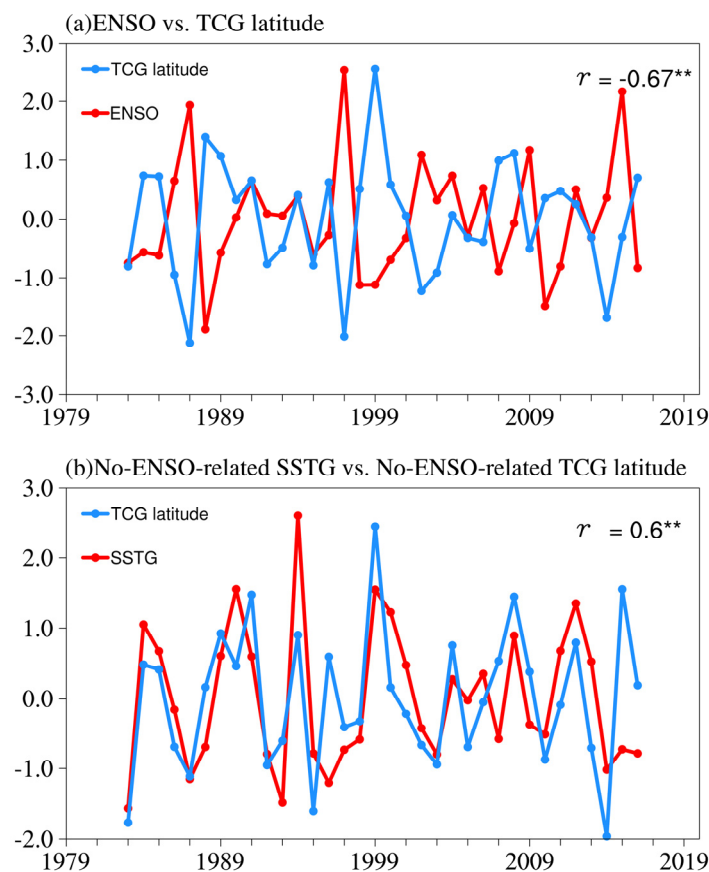


**Figure 3.** Interannual standardized time series of July–October mean (a) TCG latitude (blue line) and ENSO (red line) and (b) No-ENSO-related TCG latitude (blue line) and No-ENSO-related SSTG (red line) from 1979 to 2020. Two asterisks (\*\*) indicate that the correlation coefficients are significant at the 99% confidence level.

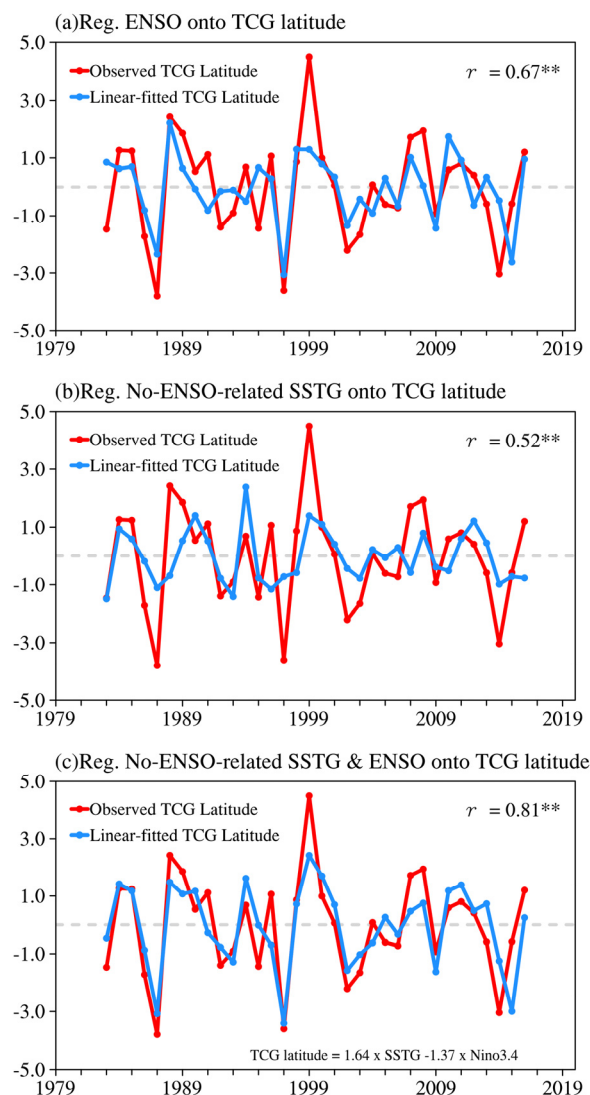


**Figure 4.** Interannual standardized time series of observed TCG latitude (red line) and multiple linear regression fits of (a) ENSO, (b) No-ENSO-related SSTG, (c) ENSO, and No-ENSO-related SSTG to the TCG latitude (blue line) from 1979 to 2020. The coefficients of the regression equation for the multiple linear regression are also shown. Two asterisks (\*\*) indicate that the correlation coefficients are significant at the 99% confidence level. Note that none of the interannual observed TCG latitude time series in the linear regression have been treated to remove ENSO.

### 3.2. Possible Physical Mechanisms

To better understand the ENSO-independent SSTG regulation of the TCG latitude, we regressed the SST field onto the ENSO-independent SSTG to obtain a clearer SST pattern. From the results in Figure 5a, we can see that the ENSO-independent SSTG well represents the north–south dipole SST gradient in the WNP region. Prior studies have confirmed that the DGPI is a good tool for diagnosing TC generation [56–58]; thus, we used the spatial correlation of the DGPI with the ENSO-independent SSTG to further explore the variation in the TC response under this meridional SST gradient (Figure 5b). Obviously, under the influence of the meridional SST difference, TC formation also shows a north–south dipole distribution. The equatorial meridional SST gradient leads to a significant increase in TC formation north of 20° N and a decrease in TC formation south of 20° N, while the poleward meridional SST gradient is the opposite. The DGPI results further support the interannual modulation of the TCG latitude by the ENSO-independent SSTG and help us to better understand the distribution of TC formation under such modulation.

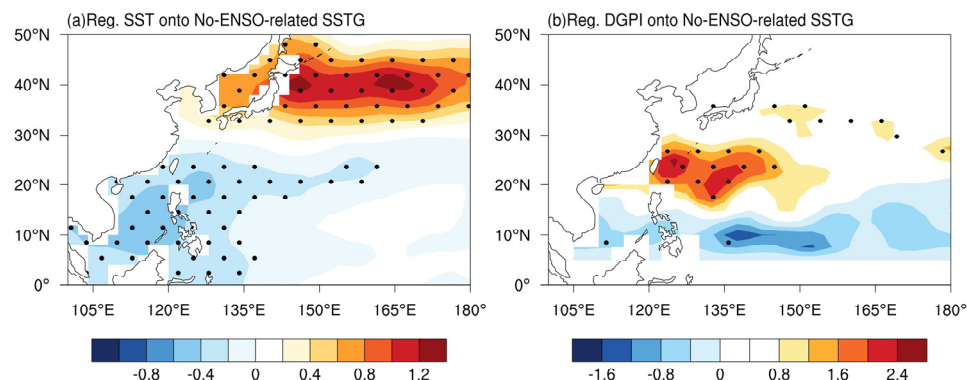


**Figure 5.** Regressed July–October mean (a) SST and (b) DGPI from 1979 to 2020. The black dots indicate significant regressions at the 95% confidence level.

Gary (1968) [1] proposed six necessary conditions affecting TC generation based on previous studies: (a) sufficient ocean heat, i.e., an SST higher than 26 °C; (b) high humidity in the middle layer (700hPa); (c) unstable atmospheric conditions; (d) a large low-level relative vorticity; (e) weak vertical wind shear; and (f) a Coriolis parameter that is too small, generally deviating from the equator by at least 5 degrees of latitude; however, these factors are not independent of each other [63]. The ocean, as a huge “energy reservoir”, constantly exchanges water vapor and energy with the atmosphere through sea–air interactions. Studies based on satellite data have shown that, on a small scale and mesoscale, SST is positively correlated with surface wind speed [64–66]. Warm SST disturbances induce boundary-layer atmospheric instability [67], significant increases in surface wind speeds and stresses, and changes in the vorticity and divergence fields associated with the crosswind and downwind components of the SST gradient [64,68–73]. On a large scale, the ocean can drive an anomalous response from the boundary-layer atmosphere through oceanic mesoscale eddies [74], hence regulating the distribution of surface winds, pressure, and convection [75–77], while the large-scale atmospheric circulation also modulates the SST and turbulent mixing in the upper ocean through wind-driven evapotranspiration [78]. Since TCs are products of air–sea interactions, the SST and its accompanying environmental factors significantly regulate TC generation, intensity, and track [79–84]. Given the important role of the SST in regulating the atmosphere and TCs, a question arises: how does the SSTG, which is not associated with ENSO, regulate the north–south distribution of TC formation?

The previous section of this study focused on a statistical understanding of the link between the TCG latitude and the ENSO-independent SSTG; however, the essential dynamical drivers and physical mechanisms remain unclear. In order to investigate the physical mechanism of the ENSO-independent SSTG affecting TCG latitude variation on interannual time scales, we regressed the July–October mean atmospheric environmental field onto the ENSO-independent SSTG (Figure 6). A clear tripolar vorticity distribution pattern, i.e., an anticyclone–cyclone–anticyclone distribution pattern, is shown in the WNP, which is similar to the typical P–J telecorrelation pattern (Figure 6a). The P–J pattern is a pressure north–south oscillation between the WNP and Japan [51,52], which has a significant influence on the East Asian summer monsoon [85–87] and TC activity [42,88–90]. Since the P–J telecorrelation is more prominent in pattern characteristics at 850 hPa, we performed the same regression for the 850 hPa vorticity field using the P–J index defined by Wakabayashi and Kawamura (2004) [53]. As expected, the circulation response excited by the P–J index is similar to the ENSO-independent SSTG (Figure 6a,b). Furthermore, the strong correlation of the P–J index with the ENSO-independent SSTG ( $r = 0.62$ ) and the TCG latitude ( $r = 0.52$ ) further suggests that the P–J telecorrelation pattern may be the cause of the ENSO-independent SSTG modulation of interannual TCG latitude variability (Figure 7) [42–44].

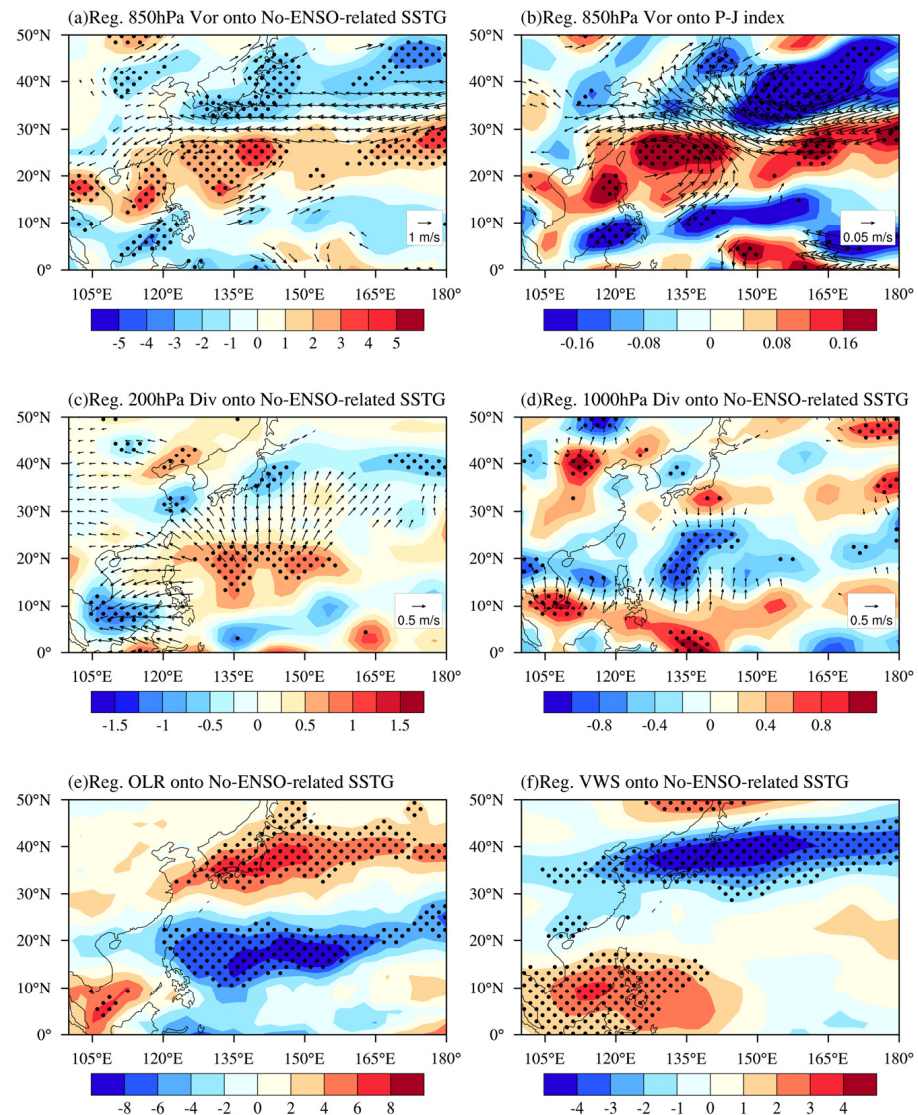


**Figure 6.** Regressed July–October mean (a) 850 hPa vorticity (shaded) and wind (vector); (c) 200 hPa divergence (shaded) and divergent wind (vector); (d) 1000 hPa divergence (shaded) and divergent wind (vector); (e) OLR; and (f) 200–850 hPa vertical wind shear onto No-ENSO-related SSTG on the interannual time scale from 1979 to 2020. (b) As in (a), but for the P-J index. The black vector and dots indicate significant regressions at the 95% confidence level.

By comparing the spatial distribution of the triple-vortex pattern over the WNP with the DGPI, it is easy to discover that the response of the P-J telecorrelation pattern to the ENSO-independent SSTG corresponds to the spatial distribution of the DGPI, with a distinct cyclonic vortex near 20° N, accompanied by convergence in the lower layer at 1000 hPa and divergence in the upper layer at 200 hPa (Figure 6c,d). Under this pumping effect of upper- and lower-level cooperation, convection developed vigorously near 20° N (Figure 6e), guiding more TCs to be generated north of 20° N. On the contrary, the low-latitude region south of 20° N had an anticyclonic vortex with significant sink airflow and enhanced vertical wind shear (Figure 6f), which is unfavorable for the maintenance of the warm core structure of TCs [1]. Therefore, the WNP TCs show a significant north–south dipole distribution under the influence of the P-J telecorrelation, with more TC generation in the WNP north of 20° N than south of 20° N.

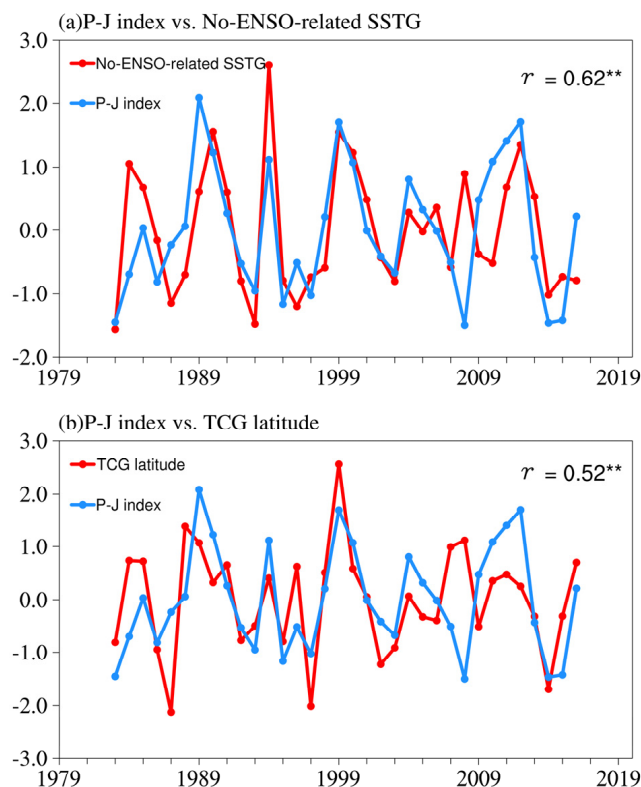


**Figure 7.** Interannual standardized time series of July–October mean (a) P-J index (blue line) and No-ENSO-related SSTG (red line) and (b) P-J index (blue line) and TCG latitude (red line) from 1979 to 2020. Two asterisks (\*\*) indicate that the correlation coefficients are significant at the 99% confidence level.

In order to further explore the origin and propagation direction of the Rossby waves excited by the P-J pattern, we regressed the 200 hPa and 850 hPa vorticity and wave activity flux onto the ENSO-independent SSTG. The regression results of the WAF in Figure 8 show that the fluctuations originate in the WNP region near the equator and propagate northward at 850 hPa. In contrast, the Rossby wave train propagates southward in the upper 200 hPa. We found that such ENSO-independent SSTG-inspired Rossby wave trains propagate in a consistent way with typical P-J propagation [87]. Indeed, previous studies have confirmed the relationship between SST anomalies and P-J formation in many oceanic regions, such as the Maritime Continent [91] and the tropical Indian Ocean [38,92]. Here, to further explore how this meridional SST difference excites the P-J pattern, we calculated the response of the geopotential height field to the ENSO-independent SSTG (Figure 9). It can be seen that under the influence of the north–south dipole meridional SST, there is a significant high-pressure anomaly over the KE region in the upper troposphere and a low-pressure anomaly over the WNP region. This suggests that under the diabatic heating effect of the warm SST in the KE region, the air expanded to rise, forming a high-pressure anomaly at a high level and diverging outward. The divergent flows converge and sink over the WNP near the equator, forming a low-pressure anomaly. This strong downwelling seems to be the main reason for triggering the formation of the P-J pattern. In other words, the meridional SST gradient triggers the P-J pattern by altering the local circulation anomalies and forms a Rossby wave train propagating northward in the lower troposphere. Consequently, a triple-vortex, anticyclone–cyclone–anticyclone pattern is formed over the WNP, directing more TCs to be generated north of 20° N.

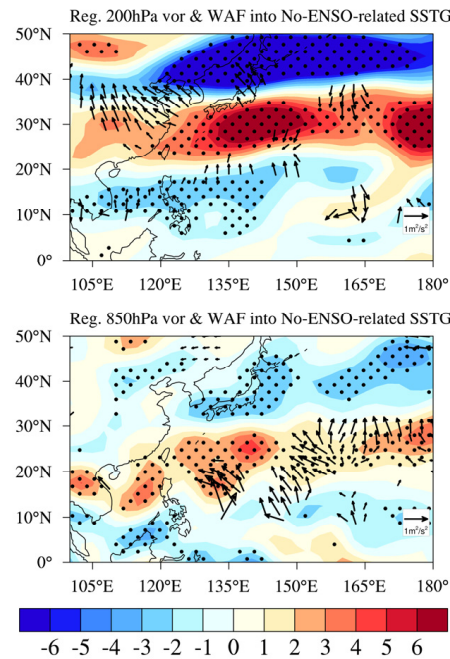


**Figure 8.** Regressed July–October mean (top) 200 hPa and (bottom) 850 hPa vorticity (shaded) and wave active flux (vector) onto ENSO-independent SSTG on the interannual time scale from 1979 to 2020. The black vector and dots indicate significant regressions at the 95% confidence level.

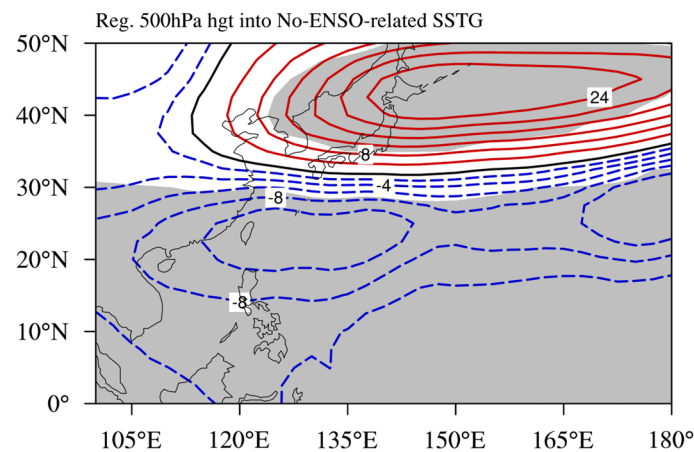


**Figure 9.** Regressed July–October mean 500 hPa geopotential height onto ENSO-independent SSTG on the interannual time scale from 1979 to 2020. The red and blue lines indicate geopotential height anomalies greater than 0 and less than 0, respectively. The gray shading indicates significant regressions at the 95% confidence level. The numbers in the figure represent the regression coefficients of the ENSO-independent SSTG regression to the geopotential height fields.

#### 4. Conclusions

ENSO is the largest interannual predictable source of TCG latitude, so previous studies on the relationship between SST variability and TCG latitude have mainly focused on the ENSO signal [27,28,46]. Although a number of studies have also mentioned the influence of other basins on TCG latitude [38,39], less emphasis has been put on the role of SST independent of the ENSO signal. Therefore, this study mainly explores the effect of the SST factor, independent of ENSO, on the interannual variability in TCG latitude. We found that the meridional SST difference between the Kuroshio Extension (KE) and the WNP region still has an effect on the interannual variability in the TCG latitude after removing the effect of the ENSO signal, as indicated by the positive and negative dipole correlation in the KE region and the WNP region. We therefore defined the ENSO-independent SST

gradient to explore its relationship with the interannual variability in the TCG latitude. We found that while ENSO remains the largest contributor to the interannual variability in the TCG latitude ( $r = -0.67$ ), the ENSO-independent SSTG also plays an important role ( $r = 0.6$ ). In addition, the participation of the ENSO-independent SSTG as a new predictor significantly improves the interannual forecasting of the TCG latitude from 0.67 to 0.81, increasing the explained variance by 20.7%. These findings emphasize the influence of the ENSO-independent SSG on interannual TCG latitude variations.

We next further explored how the ENSO-independent SSTG modulates the interannual variation in the TCG latitude and proposed a physical mechanism independent of ENSO. From the DGPI spatial distribution, it was found that the TC generation associated with the meridional SSTG shows a north–south dipole distribution, with a significant increase in TC generation near 20° N. This is mainly attributed to the P-J teleconnection pattern excited by the ENSO-independent SSTG. Under the diabatic heating effect of the warm SST in the KE region, the air expanded to rise, forming a high-pressure anomaly at a high level and diverging outward. The divergent flows converged and sank over the WNP near the equator, forming a low-pressure anomaly. This strong downwelling triggered the P-J pattern and formed a northward propagating Rossby wave train in the lower troposphere. Consequently, a triple-vortex, anticyclone–cyclone–anticyclone pattern was formed over the WNP. Under the pumping effect of upper- and lower-level cooperation, the cyclonic vortex around 20° N was enhanced, with a vigorous development of convection directing more TC generation north of 20° N. The results of this study provide a new perspective on the prediction of the interannual variability in TCG latitude. Finally, it is worth noting that the results in this paper are based on statistical analysis and need to be further confirmed through the use of numerical models and more observational analysis.

**Author Contributions:** Conceptualization, D.J. and H.Z.; analysis, D.J. and H.Z.; methodology, D.J., H.Z., M.L. and R.W.; writing, D.J., H.Z., M.L. and R.W. All authors have read and agreed to the published version of the manuscript.

**Funding:** This work was funded by the Ningbo Key R&D Program (2023Z217) and Guangxi Natural Science Foundation Project (2023GXNSFAA026511).

**Institutional Review Board Statement:** Not applicable.

**Informed Consent Statement:** Not applicable.

**Data Availability Statement:** The JTWC best track dataset is available at <https://www.metoc.navy.mil/jtwc/> (accessed on 12 May 2023). The NOAA ERSST-V5 data are available at Extended Reconstructed SST | National Centers for Environmental Information (NCEI) ([noaa.gov](https://www.noaa.gov)) (accessed on 12 May 2023). The NCEP-DOE Reanalysis 2 monthly mean reanalysis is available at NCEP/DOE Reanalysis II: NOAA Physical Sciences Laboratory NCEP/DOE Reanalysis II (accessed on 12 May 2023). The OLR data is available at CPC Daily Blended Outgoing Longwave Radiation (OLR)-2.5 degree: NOAA Physical Sciences Laboratory CPC Daily Blended Outgoing Longwave Radiation (OLR)-2.5 degree (accessed on 12 May 2023). The Niño-3.4 index is available at [https://psl.noaa.gov/gcos\\_wgsp/Timeseries/Nino34/](https://psl.noaa.gov/gcos_wgsp/Timeseries/Nino34/) (accessed on 12 May 2023).

**Conflicts of Interest:** Ronghe Wang is an employee of Nanjing Delta Water Institute. The paper reflects the views of the scientist and not the company.

## References

1. Gray, W.M. Global View of the Origin of Tropical Disturbances and Storms. *Mon. Weather Rev.* **1968**, *96*, 669–700. [[CrossRef](#)]
2. Schreck, C.J.; Knapp, K.R.; Kossin, J.P. The Impact of Best Track Discrepancies on Global Tropical Cyclone Climatologies using IBTrACS. *Mon. Weather Rev.* **2014**, *142*, 3881–3899. [[CrossRef](#)]
3. Chan, J.C.L. Tropical Cyclone Activity in the Northwest Pacific in Relation to the El Niño/Southern Oscillation Phenomenon. *Mon. Weather Rev.* **1985**, *113*, 599–606. [[CrossRef](#)]
4. Peduzzi, P.; Chatenoux, B.; Dao, H.; De Bono, A.; Herold, C.; Kossin, J.; Mouton, F.; Nordbeck, O. Global trends in tropical cyclone risk. *Nat. Clim. Chang.* **2012**, *2*, 289–294. [[CrossRef](#)]
5. Liu, K.S.; Chan, J.C.L. Inactive period of western North Pacific tropical cyclone activity in 1998–2011. *J. Clim.* **2013**, *26*, 2614–2630. [[CrossRef](#)]

6. Zhao, H.; Wang, C. Interdecadal modulation on the relationship between ENSO and typhoon activity during the late season in the western north Pacific. *Clim. Dyn.* **2016**, *47*, 315–328. [[CrossRef](#)]
7. Roy, C.; Kovordányi, R. Tropical cyclone track forecasting techniques—A review. *Atmos. Res.* **2012**, *104*, 40–69. [[CrossRef](#)]
8. Zhao, H.; Wu, L.; Zhou, W. Assessing the influence of the ENSO on tropical cyclone prevailing tracks in the western North Pacific. *Adv. Atmos. Sci.* **2010**, *27*, 1361–1371. [[CrossRef](#)]
9. Zhao, H.; Wu, L.; Zhou, W. Interannual changes of tropical cyclone intensity in the western north Pacific. *J. Meteorol. Soc. Jpn. Ser. II* **2011**, *89*, 243–253. [[CrossRef](#)]
10. Cai, Y.; Han, X.; Zhao, H.; Klotzbach, P.J.; Wu, L.; Raga, G.B.; Wang, C. Enhanced predictability of rapidly intensifying tropical cyclones over the western North Pacific associated with snow depth changes over the Tibetan Plateau. *J. Clim.* **2022**, *35*, 2093–2110. [[CrossRef](#)]
11. Yamaguchi, M.; Vitart, F.; Lang, S.T.K.; Magnusson, L.; Elsberry, R.L.; Elliott, G.; Kyouda, M.; Nakazawa, T. Global distribution of the skill of tropical cyclone activity forecasts on short-to medium-range time scales. *Weather Forecast.* **2015**, *30*, 1695–1709. [[CrossRef](#)]
12. Kossin, J.P.; Emanuel, K.A.; Vecchi, G.A. The poleward migration of the location of tropical cyclone maximum intensity. *Nature* **2014**, *509*, 349–352. [[CrossRef](#)] [[PubMed](#)]
13. Daloz, A.S.; Camargo, S.J. Is the poleward migration of tropical cyclone maximum intensity associated with a poleward migration of tropical cyclone genesis? *Clim. Dyn.* **2018**, *50*, 705–715. [[CrossRef](#)]
14. Zhao, H.; Duan, X.; Raga, G.B.; Klotzbach, P.J. Changes in characteristics of rapidly intensifying western North Pacific tropical cyclones related to climate regime shifts. *J. Clim.* **2018**, *31*, 8163–8179. [[CrossRef](#)]
15. Wu, L.; Wang, C.; Wang, B. Westward shift of western North Pacific tropical cyclogenesis. *Geophys. Res. Lett.* **2015**, *42*, 1537–1542. [[CrossRef](#)]
16. He, H.; Yang, J.; Gong, D.; Mao, R.; Wang, Y.; Gao, M. Decadal changes in tropical cyclone activity over the western North Pacific in the late 1990s. *Clim. Dyn.* **2015**, *45*, 3317–3329. [[CrossRef](#)]
17. Korty, R.L.; Emanuel, K.A.; Huber, M.; Zamora, R.A. Tropical cyclones downscaled from simulations with very high carbon dioxide levels. *J. Clim.* **2017**, *30*, 649–667. [[CrossRef](#)]
18. Kossin, J.P.; Emanuel, K.A.; Camargo, S.J. Past and projected changes in western North Pacific tropical cyclone exposure. *J. Clim.* **2016**, *29*, 5725–5739. [[CrossRef](#)]
19. Bell, S.S.; Chand, S.S.; Tory, K.J.; Dowdy, A.J.; Turville, C.; Ye, H. Projections of southern hemisphere tropical cyclone track density using CMIP5 models. *Clim. Dyn.* **2019**, *52*, 6065–6079. [[CrossRef](#)]
20. Shan, K.; Yu, X. Enhanced understanding of poleward migration of tropical cyclone genesis. *Environ. Res. Lett.* **2020**, *15*, 104062. [[CrossRef](#)]
21. Song, J.; Klotzbach, P.J. What has controlled the poleward migration of annual averaged location of tropical cyclone lifetime maximum intensity over the western North Pacific since 1961? *Geophys. Res. Lett.* **2018**, *45*, 1148–1156. [[CrossRef](#)]
22. Moon, I.-J.; Kim, S.-H.; Klotzbach, P.; Chan, J.C.L. Roles of interbasin frequency changes in the poleward shifts of the maximum intensity location of tropical cyclones. *Environ. Res. Lett.* **2015**, *10*, 104004. [[CrossRef](#)]
23. Li, T.; Kwon, M.; Zhao, M.; Kug, J.; Luo, J.; Yu, W. Global warming shifts Pacific tropical cyclone location. *Geophys. Res. Lett.* **2010**, *37*, L21804. [[CrossRef](#)]
24. Knutson, T.; Camargo, S.J.; Chan, J.C.L.; Emanuel, K.; Ho, C.-H.; Kossin, J.; Mohapatra, M.; Satoh, M.; Sugi, M.; Walsh, K.; et al. Tropical cyclones and climate change assessment: Part I: Detection and attribution. *Bull. Am. Meteorol. Soc.* **2019**, *100*, 1987–2007. [[CrossRef](#)]
25. Lee, C.Y.; Camargo, S.J.; Sobel, A.H.; Tippett, M.K. Statistical–dynamical downscaling projections of tropical cyclone activity in a warming climate: Two diverging genesis scenarios. *J. Clim.* **2020**, *33*, 4815–4834. [[CrossRef](#)]
26. Gray, W.M. Atlantic seasonal hurricane frequency. Part I: El Niño and 30 mb quasi-biennial oscillation influences. *Mon. Weather Rev.* **1984**, *112*, 1649–1668. [[CrossRef](#)]
27. Wang, B.; Chan, J.C.L. How strong ENSO events affect tropical storm activity over the western North Pacific. *J. Clim.* **2002**, *15*, 1643–1658. [[CrossRef](#)]
28. Camargo, S.J.; Sobel, A.H. Western North Pacific tropical cyclone intensity and ENSO. *J. Clim.* **2005**, *18*, 2996–3006. [[CrossRef](#)]
29. Chia, H.H.; Ropelewski, C.F. The interannual variability in the genesis location of tropical cyclones in the northwest Pacific. *J. Clim.* **2002**, *15*, 2934–2944. [[CrossRef](#)]
30. Wang, X.; Zhou, W.; Li, C.; Wang, D. Effects of the East Asian summer monsoon on tropical cyclone genesis over the South China Sea on an interdecadal time scale. *Adv. Atmos. Sci.* **2012**, *29*, 249–262. [[CrossRef](#)]
31. Li, R.C.Y.; Zhou, W. Changes in western Pacific tropical cyclones associated with the El Niño–Southern Oscillation cycle. *J. Clim.* **2012**, *25*, 5864–5878. [[CrossRef](#)]
32. Ashok, K.; Behera, S.K.; Rao, S.A.; Weng, H.; Yamagata, T. El Niño Modoki and its possible teleconnection. *J. Geophys. Res. Ocean* **2007**, *112*. [[CrossRef](#)]
33. Yu, J.Y.; Kao, H.Y. Decadal Changes of ENSO Persistence Barrier in SST and Ocean Heat Content Indices: 1958–2001. *J. Geophys. Res.* **2007**, *112*, D13106. [[CrossRef](#)]
34. Wang, C.; Li, C.; Mu, M.; Duan, W. Seasonal modulations of different impacts of two types of ENSO events on tropical cyclone activity in the western North Pacific. *Clim. Dyn.* **2013**, *40*, 2887–2902. [[CrossRef](#)]

35. Saji, N.H.; Yamagata, T. Possible impacts of Indian Ocean dipole mode events on global climate. *Clim. Res.* **2003**, *25*, 151–169. [[CrossRef](#)]
36. Yoo, S.H.; Yang, S.; Ho, C.H. Variability of the Indian Ocean sea surface temperature and its impacts on Asian-Australian monsoon climate. *J. Geophys. Res. Atmos.* **2006**, *111*, D03108. [[CrossRef](#)]
37. Yang, J.; Liu, Q.; Xie, S.; Liu, Z.; Wu, L. Impact of the Indian Ocean SST basin mode on the Asian summer monsoon. *Geophys. Res. Lett.* **2007**, *34*, L02708. [[CrossRef](#)]
38. Xie, S.P.; Hu, K.; Hafner, J.; Tokinaga, H.; Du, Y.; Huang, G.; Sampe, T. Indian Ocean capacitor effect on Indo–western Pacific climate during the summer following El Niño. *J. Clim.* **2009**, *22*, 730–747. [[CrossRef](#)]
39. Du, Y.; Yang, L.; Xie, S.P. Tropical Indian Ocean influence on northwest Pacific tropical cyclones in summer following strong El Niño. *J. Clim.* **2011**, *24*, 315–322. [[CrossRef](#)]
40. Gong, H.; Wang, L.; Chen, W.; Wu, R.; Huang, G.; Nath, D. Diversity of the Pacific–Japan pattern among CMIP5 models: Role of SST anomalies and atmospheric mean flow. *J. Clim.* **2018**, *31*, 6857–6877. [[CrossRef](#)]
41. Tao, L.; Li, T.; Ke, Y.H.; Zhao, J.W. Causes of interannual and interdecadal variations of the summertime Pacific–Japan-like pattern over East Asia. *J. Clim.* **2017**, *30*, 8845–8864. [[CrossRef](#)]
42. Choi, K.S.; Wu, C.C.; Cha, E.J. Change of tropical cyclone activity by Pacific–Japan teleconnection pattern in the western North Pacific. *J. Geophys. Res. Atmos.* **2010**, *115*, D19114. [[CrossRef](#)]
43. Zhan, R.; Wang, Y.; Lei, X. Contributions of ENSO and East Indian Ocean SSTA to the interannual variability of Northwest Pacific tropical cyclone frequency. *J. Clim.* **2011**, *24*, 509–521. [[CrossRef](#)]
44. Chen, G.; Tam, C.Y. Different impacts of two kinds of Pacific Ocean warming on tropical cyclone frequency over the western North Pacific. *Geophys. Res. Lett.* **2010**, *37*, L01803. [[CrossRef](#)]
45. Jiayu, Z.; Wu, Q.; Guo, Y.; Zhao, S. The impact of summertime North Indian ocean SST on tropical cyclone genesis over the Western North Pacific. *Sola* **2016**, *12*, 242–246. [[CrossRef](#)]
46. Camargo, S.J.; Emanuel, K.A.; Sobel, A.H. Use of a genesis potential index to diagnose ENSO effects on tropical cyclone genesis. *J. Clim.* **2007**, *20*, 4819–4834. [[CrossRef](#)]
47. Wang, H.J.; Sun, J.Q.; Fan, K. Relationships between the North Pacific Oscillation and the typhoon/hurricane frequencies. *Sci. China Ser. D Earth Sci.* **2007**, *50*, 1409–1416. [[CrossRef](#)]
48. Chu, P.S. Large-scale circulation features associated with decadal variations of tropical cyclone activity over the central North Pacific. *J. Clim.* **2002**, *15*, 2678–2689. [[CrossRef](#)]
49. Huang, S.; Oey, L.Y. Land-falling typhoons are controlled by the meridional oscillation of the Kuroshio Extension. *Clim. Dyn.* **2019**, *52*, 2855–2867. [[CrossRef](#)]
50. Kanamitsu, M.; Ebisuzaki, W.; Woollen, J.; Yang, S.-K.; Hnilo, J.J.; Fiorino, M.; Potter, G.L. Ncep–doe amip–ii reanalysis (r-2). *Bull. Am. Meteorol. Soc.* **2002**, *83*, 1631–1644. [[CrossRef](#)]
51. Huang, R.H.; Li, W.J. Influence of heat source anomaly over the western tropical Pacific on the subtropical high over East Asia and its physical mechanism. *Chin. J. Atmos. Sci.* **1988**, *12*, 107–116.
52. Nitta, T. Long-term variations of cloud amount in the western Pacific region. *J. Meteorol. Soc. Jpn. Ser. II* **1986**, *64*, 373–390. [[CrossRef](#)]
53. Wakabayashi, S.; Kawamura, R. Extraction of major teleconnection patterns possibly associated with the anomalous summer climate in Japan. *J. Meteorol. Soc. Jpn. Ser. II* **2004**, *82*, 1577–1588. [[CrossRef](#)]
54. Takaya, K.; Nakamura, H. A formulation of a phase-independent wave-activity flux for stationary and migratory quasigeostrophic eddies on a zonally varying basic flow. *J. Atmos. Sci.* **2001**, *58*, 608–627. [[CrossRef](#)]
55. Emanuel, K.; Nolan, D.S. Tropical cyclone activity and the global climate system. In Proceedings of the 26th Conference on Hurricanes and Tropical Meteorology, Miami, FL, USA, 3–7 May 2004; American Meteorology Society: Boston, MA, USA, 2004; Volume 10, pp. 240–241.
56. Cao, J.; Zhao, H.; Wang, B.; Wu, L. Hemisphere-asymmetric tropical cyclones response to anthropogenic aerosol forcing. *Nat. Commun.* **2021**, *12*, 6787. [[CrossRef](#)] [[PubMed](#)]
57. Cao, J.; Wang, H.; Zhao, H.; Wang, B.; Wu, L.; Wang, C. Reversed and comparable climate impacts from historical anthropogenic aerosol and GHG on global-scale tropical cyclone genesis potential. *Environ. Res. Lett.* **2022**, *17*, 094027. [[CrossRef](#)]
58. Murakami, H.; Wang, B. Patterns and frequency of projected future tropical cyclone genesis are governed by dynamic effects. *Commun. Earth Environ.* **2022**, *3*, 77. [[CrossRef](#)]
59. Wang, B.; Murakami, H. Dynamic genesis potential index for diagnosing present-day and future global tropical cyclone genesis. *Environ. Res. Lett.* **2020**, *15*, 114008. [[CrossRef](#)]
60. Ashok, K.; Guan, Z.; Yamagata, T. A look at the relationship between the ENSO and the Indian Ocean dipole. *J. Meteorol. Soc. Jpn. Ser. II* **2003**, *81*, 41–56. [[CrossRef](#)]
61. Shindell, D.; Faluvegi, G.J.N.G. Climate response to regional radiative forcing during the twentieth century. *Nat. Geosci.* **2009**, *2*, 294–300. [[CrossRef](#)]
62. Li, C. Actions of typhoons over the western Pacific (including the South China Sea) and El Niño. *Adv. Atmos. Sci.* **1988**, *5*, 107–115. [[CrossRef](#)]
63. Frank, W.M. Tropical cyclone formation. In *A Global View of Tropical Cyclones*; Office of Naval Research: Arlington, VA, USA, 1987; pp. 53–90.

64. Chelton, D.B.; Esbensen, S.K.; Schlax, M.G.; Thum, N.; Freilich, M.H.; Wentz, F.J.; Gentemann, C.L.; McPhaden, M.J.; Schopf, P.S. Observations of coupling between surface wind stress and sea surface temperature in the eastern tropical Pacific. *J. Clim.* **2001**, *14*, 1479–1498. [[CrossRef](#)]
65. Liu, T.W.; Xie, X.; Polito, P.S.; Xie, S.; Hashizume, H. Atmospheric manifestation of tropical instability wave observed by QuikSCAT and Tropical Rain Measuring Mission. *Geophys. Res. Lett.* **2000**, *27*, 2545–2548. [[CrossRef](#)]
66. Hashizume, H.; Xie, S.P.; Liu, W.T.; Takeuchi, K. Local and remote atmospheric response to tropical instability waves: A global view from space. *J. Geophys. Res. Atmos.* **2001**, *106*, 10173–10185. [[CrossRef](#)]
67. Ricchi, A.; Sangelantoni, L.; Redaelli, G.; Mazzarella, V.; Montopoli, M.; Miglietta, M.M.; Tiesi, A.; Mazzà, S.; Rotunno, R.; Ferretti, R. Impact of the SST and topography on the development of a large-hail storm event, on the Adriatic Sea. *Atmos. Res.* **2023**, *296*, 107078. [[CrossRef](#)]
68. Chelton, D.B.; Schlax, M.G.; Samelson, R.M. Summertime coupling between sea surface temperature and wind stress in the California Current System. *J. Phys. Oceanogr.* **2007**, *37*, 495–517. [[CrossRef](#)]
69. Chelton, D.B. The impact of SST specification on ECMWF surface wind stress fields in the eastern tropical Pacific. *J. Clim.* **2005**, *18*, 530–550. [[CrossRef](#)]
70. O’Neill, L.W.; Chelton, D.B.; Esbensen, S.K. The effects of SST-induced surface wind speed and direction gradients on midlatitude surface vorticity and divergence. *J. Clim.* **2010**, *23*, 255–281. [[CrossRef](#)]
71. O’Neill, L.W.; Chelton, D.B.; Esbensen, S.K.; Wentz, F.J. High-resolution satellite measurements of the atmospheric boundary layer response to SST variations along the Agulhas Return Current. *J. Clim.* **2005**, *18*, 2706–2723. [[CrossRef](#)]
72. O’Neill, L.W.; Chelton, D.B.; Esbensen, S.K. Observations of SST-induced perturbations of the wind stress field over the Southern Ocean on seasonal timescales. *J. Clim.* **2003**, *16*, 2340–2354. [[CrossRef](#)]
73. Meroni, A.N.; Parodi, A.; Pasquero, C. Role of SST patterns on surface wind modulation of a heavy midlatitude precipitation event. *J. Geophys. Res. Atmos.* **2018**, *123*, 9081–9096. [[CrossRef](#)]
74. Small, R.; Deszoeke, S.; Xie, S.; O’Neill, L.; Seo, H.; Song, Q.; Cornillon, P.; Spall, M.; Minobe, S. Air–sea interaction over ocean fronts and eddies. *Dyn. Atmos. Ocean.* **2008**, *45*, 274–319. [[CrossRef](#)]
75. Miyamoto, A.; Nakamura, H.; Miyasaka, T. Influence of the subtropical high and storm track on low-cloud fraction and its seasonality over the south Indian Ocean. *J. Clim.* **2018**, *31*, 4017–4039. [[CrossRef](#)]
76. Frenger, I.; Gruber, N.; Knutti, R.; Münnich, M. Imprint of Southern Ocean eddies on winds, clouds and rainfall. *Nat. Geosci.* **2013**, *6*, 608–612. [[CrossRef](#)]
77. Seo, H.; O’Neill, L.W.; Bourassa, M.A.; Czaja, A.; Drushka, K.; Edson, J.B.; Fox-Kemper, B.; Frenger, I.; Gille, S.T.; Kirtman, B.P.; et al. Ocean mesoscale and frontal-scale ocean–atmosphere interactions and influence on large-scale climate: A review. *J. Clim.* **2023**, *36*, 1981–2013. [[CrossRef](#)]
78. Small, R.J.; de Szoeke, S.; Xie, S.P.; O’Neill, L.; Seo, H.; Song, Q.; Cornillon, P.; Spall, M.; Minobe, S. Atmospheric response to ocean fronts and eddies: A Review. In Proceedings of the 15th Conference on Air-Sea Interaction, Portland, OR, USA, 20–24 August 2007.
79. Rotunno, R.; Emanuel, K.A. An air–sea interaction theory for tropical cyclones. Part II: Evolutionary study using a nonhydrostatic axisymmetric numerical model. *J. Atmos. Sci.* **1987**, *44*, 542–561. [[CrossRef](#)]
80. Zambon, J.B.; He, R.; Warner, J.C. Investigation of hurricane Ivan using the coupled ocean–atmosphere–wave–sediment transport (COAWST) model. *Ocean. Dyn.* **2014**, *64*, 1535–1554. [[CrossRef](#)]
81. Everson DA, L.; Gan, M.A.; de Lima MOSCATIM, C. The role of latent and sensible heat fluxes in an explosive cyclogenesis over the South American East Coast. *J. Meteorol. Soc. Jpn.* **2011**, *89*, 637–663. [[CrossRef](#)]
82. Carniel, S.; Benetazzo, A.; Bonaldo, D.; Falcieri, F.M.; Miglietta, M.M.; Ricchi, A.; Sclavo, M. Scratching beneath the surface while coupling atmosphere, ocean and waves: Analysis of a dense water formation event. *Ocean Model.* **2016**, *101*, 101–112. [[CrossRef](#)]
83. Tous, M.; Romero, R.; Ramis, C. Surface heat fluxes influence on medicane trajectories and intensification. *Atmos. Res.* **2013**, *123*, 400–411. [[CrossRef](#)]
84. Warner, J.C.; Armstrong, B.; He, R.; Zambon, J.B. Development of a coupled ocean–atmosphere–wave–sediment transport (COAWST) modeling system. *Ocean Model.* **2010**, *35*, 230–244. [[CrossRef](#)]
85. Huang, R.; Sun, F. Impacts of the tropical western Pacific on the East Asian summer monsoon. *J. Meteorol. Soc. Jpn. Ser. II* **1992**, *70*, 243–256. [[CrossRef](#)]
86. Kosaka, Y.; Nakamura, H. Structure and dynamics of the summertime Pacific–Japan teleconnection pattern. *Q. J. R. Meteorol. Soc. A J. Atmos. Sci. Appl. Meteorol. Phys. Oceanogr.* **2006**, *132*, 2009–2030. [[CrossRef](#)]
87. Huang, R.; Chen, J.; Wang, L.; Lin, Z. Characteristics, processes, and causes of the spatio-temporal variabilities of the East Asian monsoon system. *Adv. Atmos. Sci.* **2012**, *29*, 910–942. [[CrossRef](#)]
88. Kim, J.S.; Li, R.C.Y.; Zhou, W. Effects of the Pacific–Japan teleconnection pattern on tropical cyclone activity and extreme precipitation events over the Korean peninsula. *J. Geophys. Res. Atmos.* **2012**, *117*. [[CrossRef](#)]
89. Zhan, R.; Wang, Y.; Wu, C.C. Impact of SSTA in the east Indian Ocean on the frequency of northwest Pacific tropical cyclones: A regional atmospheric model study. *J. Clim.* **2011**, *24*, 6227–6242. [[CrossRef](#)]
90. Tao, L.; Wu, L.; Wang, Y.; Yang, J. Influence of tropical Indian Ocean warming and ENSO on tropical cyclone activity over the western North Pacific. *J. Meteorol. Soc. Jpn. Ser. II* **2012**, *90*, 127–144. [[CrossRef](#)]

91. Xie, M.; Wang, C.; Chen, S. The role of the Maritime Continent SST anomalies in maintaining the Pacific–Japan pattern on decadal time scales. *J. Clim.* **2022**, *35*, 1079–1095. [[CrossRef](#)]
92. Wu, B.; Zhou, T.; Li, T. Contrast of rainfall–SST relationships in the western North Pacific between the ENSO-developing and ENSO-decaying summers. *J. Clim.* **2009**, *22*, 4398–4405. [[CrossRef](#)]

**Disclaimer/Publisher’s Note:** The statements, opinions and data contained in all publications are solely those of the individual author(s) and contributor(s) and not of MDPI and/or the editor(s). MDPI and/or the editor(s) disclaim responsibility for any injury to people or property resulting from any ideas, methods, instructions or products referred to in the content.